Davide Massarotti, Thilo Bauch, Floriana Lombardi, and Francesco Tafuri

10 Josephson and charging effect in mesoscopic superconducting devices

10.1 Introduction and historical background

In this chapter we consider Josephson junctions at the submicron and nanoscale. Much progress has been made since the pioneering work on nanoscale point-contact junctions. The modern era of Josephson devices has been strongly influenced by the combined continuous progress in material science and nanotechnologies. Both have strongly influenced the development of superconducting devices based on the Josephson effect at three fundamental levels: basic physics, device and circuit innovation, and materials science and process development. Advances in nanotechnologies applied to superconductivity frequently offer solutions to relevant material science problems, for example scaling barriers and interfaces, and handling prebuilt barriers for instance in nanowires (NWs) and flakes of graphene or of a topological insulator. Hybrid junctions are an obvious consequence of the combined progress of material science and nanotechnology.

The story behind the Josephson effect [1] is marked by the use of special materials and techniques at some key moments. At the very beginning, thermal cycling stability problems for lead alloy-based junctions were definitely overcome by the use of rigid superconductors such as Nb [2, 3]. Replacement of Nb oxide barriers by artificial barriers was key in the development of Nb technology. Al was revealed as the perfect solution forming a natural, self-limiting, high-quality, insulating oxide [4]. The impact of high critical temperature superconductors (HTS) was also impressive for Josephson device development activities [5, 6]. Most of the unconventional materials since HTS have benefited from the notions and techniques developed to build HTS Josephson junctions and to handle their complexity as much as possible. This obviously includes innovative methods for building barriers in intrinsically nonhomogeneous materials. Meanwhile (in the 1990s), the advent of mesoscopic physics was changing some conceptual paradigms also in superconductivity, and more importantly nanotechnologies started offering new experimental tools to build completely new fami-

Davide Massarotti, Dipartimento di Fisica "Ettore Pancini", Università degli Studi di Napoli Federico II; CNR-SPIN, Monte S. Angelo- Via Cintia, I-80126, Napoli, Italy
Thilo Bauch, Chalmers University of Technology, SE-41296 Göteborg, Sweden
Floriana Lombardi, Chalmers University of Technology, SE-41296 Göteborg, Sweden
Francesco Tafuri, Dipartimento di Fisica "Ettore Pancini", Università degli Studi di Napoli Federico II; CNR-SPIN, Monte S. Angelo- Via Cintia, I-80126, Napoli, Italy

DOI 10.1515/9783110456806-011,

lies of devices. These techniques applied to Josephson junctions became more mature only later. Progress in material science means new materials and new superconductors, and novel abilities to build interfaces and for precise control of heterostructural growth. Also tunnel junction barriers are now designed and fabricated with unprecedented precision, opening the route to better performing devices even for technologies based on well-established low critical temperature superconductors (LTS).

In conclusion, we have never had so many different families of superconducting materials and so many different types of Josephson junctions as today, with so many fundamental open questions on their nature. Here we focus on specific aspects of the nanoscale junctions, directing the reader looking for a more detailed account of Josephson phenomenology to the traditional textbooks [2, 3] and extensive reviews [5, 6].

10.2 Brief introductory notes on the Josephson effect: main equations, scaling energies and quantum implications

Most of the common ways of placing a barrier between superconducting electrodes are shown in Figure 10.1, and will be discussed in the following. Josephson coupling can also take place at grain boundaries (GBs) [5, 6]. Josephson predicted the existence of tunnel currents carried by Cooper pairs between two superconductors S and S' separated by a thin (typically less than 1 nm) insulating layer I [1] (see Figure 10.1a) [1–3].

The two basic Josephson equations originally derived for an S-I-S' junction are:

$$I_s = I_c \sin(\phi) \,. \tag{10.1}$$

$$\dot{\phi} = 2\,\mathrm{eV}/\hbar \tag{10.2}$$

where $\phi = \phi_1 - \phi_2$ is the phase difference between the two superconducting electrodes ϕ_1 and ϕ_2, and e and $\hbar$ are the electron charge and the Planck constant, respectively. I_c is the maximum critical current. The microscopic derivation can be found in [1–3]. We have the Josephson effect as long as the macroscopic wave functions of the two electrodes overlap in the barrier region.

Coulomb $E_c = e^2/(2C)$ and Josephson $E_J = \Phi_o I_c/(2\pi)$ energies will be associated with each junction, with the flux quantum $\Phi_o = h/(2e)$. Quantum Josephson junctions (JJs) with either a well-defined charge or phase variable will depend on the relative magnitude of E_c and E_J (phase for $E_J \gg E_c$, charge for $E_J \ll E_c$, respectively) [2, 3].

The Josephson effect is also observed in junctions with more transmissive barriers (normal metal (N), semiconductors (Sm), ferromagnets (F), ...). The resulting S – N(Sm, F) – S′ structure will exhibit the Josephson effect for barrier thickness (L) of the order of the coherence length in the barrier, which is for a metal $\xi_N = (\hbar D_n/k_B T)^{1/2}$ (T is the temperature, k_B is the Boltzmann constant and $D_n = v_F l/3$ is the normal metal diffusion constant, where v_F is the Fermi velocity and l the electron mean free path,

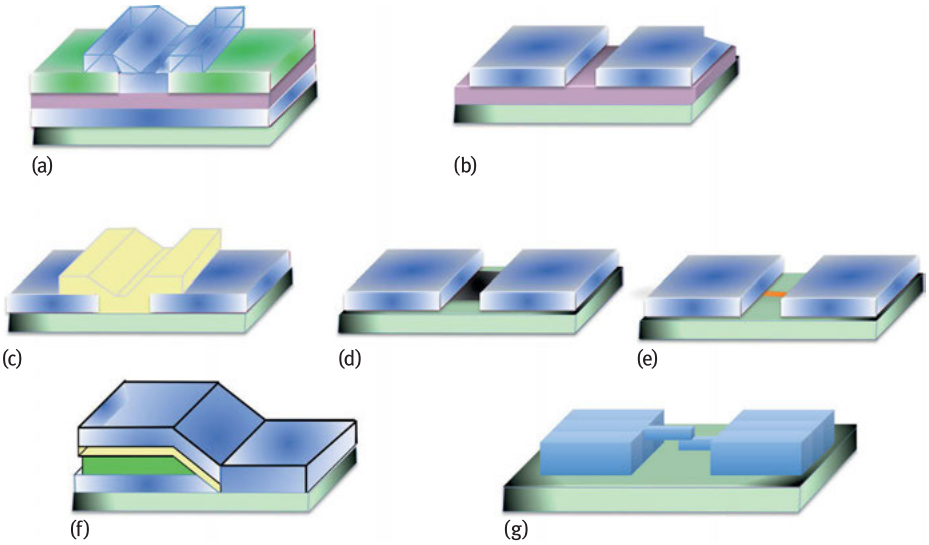

Fig. 10.1: a) Window-type geometry for a sandwich junction with insulating or normal metal barrier. The normal metal can be replaced by a semiconductor or a ferromagnetic layer. (b) Coplanar variable-thickness bridge; the barrier is grown before the deposition of the superconductor. Part of the superconducting layer is then removed to separate the two electrodes. (c) Two superconducting electrodes, grown on an insulating substrate, can be connected thorough a thin layer deposited on the top. The barrier can be a flake of graphene or of a topological insulator (d), or a nanowire (e), which in the suspended configuration can be deposited on the superconductor. In this case a trench separating the two electrodes has been previously drilled. In all these configurations one of the critical parameters is the distance between the electrodes L, which needs to be of the order of the coherence length in N, ξ_N. In (f) an edge-type variable-thickness bridge is shown. The barrier is deposited on the edge of the superconductor that has been suitably etched and treated. This configuration is particularly advantageous for the realization of submicron junctions and for devices based on anisotropic superconductors such as HTS, exploiting coherence in the a–b planes. In (g) a sketch of the layout typically used for intrinsic junctions is shown. A focussed ion beam can give a special shape to the variable-thickness bridge and oblige the current to pass through a narrow channel perpendicular to the substrate. For HTS this is intended to force the current to pass through a selected number of planes.

respectively). Apart from a dramatic change in resistance (R_n), a first obvious consequence of replacing an I with an N as a barrier is a change in the effective capacitance. New physical "processes" take place on different scaling lengths and energies, and can dominate over tunnel effects. These have been traditionally expressed in terms of the proximity effect (PE), the mutual influence of a superconducting layer in contact with a normal metal or a semiconducting or ferromagnetic layer, and in the last 20 years more and more commonly, in terms of Andreev reflection (AR) [7], the microscopic process in which a dissipative electrical current is converted at an S/N interface into a dissipationless supercurrent. The mutual influence between S and N is also con-

trolled by the nature of the interface and by the boundary conditions, which involve the respective $\xi_{N,S}$ and the thickness of the N and S layers [8, 9].

Other classical ways to form a Josephson junction exploit the concept of a tip mechanically approaching a bulk superconductor (point contact) and the more recent atomic contacts [10], or the creation of a microrestriction in a superconducting thin film [2, 3]. In this last case the Josephson effect only takes place for $L < 3.5\xi$ independently of the width W [8]. Phenomena associated with phase slips ($W < \xi$) or with the motion of Abrikosov vortices ($W > \xi$) will take place for $L > 3.5\xi$ [8].

More transmissive barriers require a more general expression of the current-phase relation:

$$I_s(\phi) = \sum_{n\geq 1} (I_n \sin(n\phi) + J_n \cos(n\phi)) \ . \tag{10.3}$$

The d.c. Josephson equation (10.1) represents the particular case of this general expression. The I_n contribution depends on the barrier transparency D as a D^n power law and corresponds to the n-multiple reflection process. The J_n vanish if time-reversal symmetry is not broken [11].

Deviations from $\sin(\phi)$ behavior are acquiring more and more importance not only because of d-wave HTS and superconductor-ferromagnet-superconductor (SFS) JJs but also for all unconventional junctions [8, 9]. The $I_s(\phi)$ relation is a characteristic Josephson "code" and is the input to define most junction parameters commonly measured in experiments. We refer for a detailed treatment and for all original references again to reviews [8, 9].

The dependence of I_c on the magnetic field is another well-defined code, widely described in textbooks [2, 3], where several anomalous behaviors have been investigated in detail. A simple example of how the magnetic response can be modified in a nanoscale hybrid junction is shown in Figure 10.2. In diffusive S–N–S junctions the Fraunhofer pattern transforms in a monotonic decay when the width of the normal wire W is smaller than the magnetic length $\xi_H = \sqrt{\Phi_0/H}$, where H is the externally applied magnetic field, as shown in Figure 10.2 [12]. This behavior is intimately related to the appearance of a linear array of vortices in the middle of the normal wire, the properties of which are very similar to those in the mixed state of a type II superconductor [12]. Edge states in wide coplanar nanojunctions (where the barrier is typically a flake of graphene or of a topological insulator) tend to transform the response in a superconducting quantum interference device (SQUID)-like pattern. HTS 0-π corner junctions offer another characteristic reference pattern with two symmetric maxima at finite H [13, 14]. When increasing the number of 0-π facets, symmetric maxima move to higher H and a number of small I_c oscillations proportional to the number of facets appear [15]. If the order parameters were to comprise an imaginary s-wave admixture, the pattern for the arrays would display distinct asymmetries, especially for low fields. A series of anomalous behaviors has been carefully classified and correlated to grain boundary morphology and intrinsic phase variation [5, 6]. Flux focusing effects can also play a relevant role and change the periodicity between two

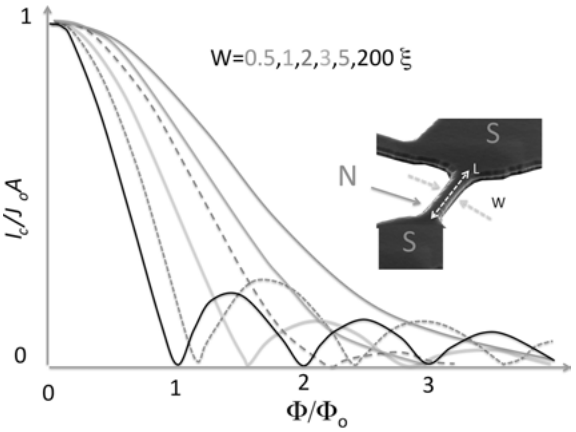

Fig. 10.2: Schematic dependence of I_c on the magnetic field for diffusive S–N–S junctions: $I_c(H)$ strongly depend on the barrier dimensions. In the inset a sketch of the junction is shown with its dimensions (partly adapted from [12]).

minima of the magnetic pattern [16, 17]. In the thin limit approximation, for instance, the effective area of the Josephson junction scales as the square of W ($\propto 1/W^2$) rather than as the usual $\propto 1/(W(2\lambda + L)$ dependence [17]. A prevailing second harmonic can also induce a dramatic change in the flux periodicity as occurring in HTS 0-π/4 grain boundary junctions [18, 19] and spin filter junctions [20, 21].

10.2.1 Josephson effect from quasiparticle Andreev-bound states

Andreev reflection (AR) is the scattering mechanism describing how an electron excitation slightly above the Fermi level in a normal metal is reflected at the interface as a hole excitation slightly below the Fermi level [7]. The missing charge of 2e is removed as a Cooper pair. This is a branch-crossing process that converts electrons into holes and vice versa, and therefore changes the net charge in the excitation distribution. The reflected hole (or electron) has a shift in phase compared to the incoming electron (or hole) wave-function: $\phi_{\text{hole}} = \phi_{\text{elect}} + \phi_{\text{superc}} + \arccos(E/\Delta)$ ($\phi_{\text{elect}} = \phi_{\text{hole}} - \phi_{\text{superc}} + \arccos(E/\Delta)$), where Δ and ϕ_{superc} are the gap value and the superconducting phase of S, respectively. The macroscopic phase of S and the microscopic phase of the quasiparticles are therefore mixed through AR. To provide an intuitive idea of the effects related to AR, the Andreev-reflected holes act as a parallel conduction channel to the initial electron current, thus doubling the normal state conductance of the S/N interface for applied voltages less than the superconducting gap $eV < \Delta$ [22]. Blonder, Tinkham and Klapwijk [22] (*BTK*) introduced the dimensionless parameter Z, proportional to the potential barrier at the interface, to describe the barrier transparency.

The Landauer conductance expression has been extended to the case of an S–N interface through scattering matrix theory [23]:

$$G_{\mathrm{NS}} = \frac{2e^2}{\pi\hbar} \sum_{n=1}^{N} \frac{D_n^2}{(2 - D_n)^2} \tag{10.4}$$

Here the D_n's are the transmission eigenvalues of the disordered normal part. The difference in the behavior of the transmission eigenvalues D_n will lead to different mesoscopic behaviors of tunnel junctions and metallic weak links. While in the former case many small D_n's are relevant, in the latter most D_n's are close to zero or unity. This expression is valid at zero voltage and zero magnetic field. Application of either a voltage or a magnetic field reduces the contact resistance of the NS junction by a factor of two.

A very interesting property of the Andreev reflection in a S_1–N–S_2 structure is that the electron obtains an extra phase of $\phi_1 - \phi_2 + \pi$ in each period. The Josephson effect can be reformulated in terms of this property and of quasiparticle bound states. The spectrum of the elementary excitations of an N layer in contact with S on both sides is quantized for $E < \Delta$. In particular the expression of the bound state energy in a S–N–S one-dimensional system, in the short junction limit $L \ll \xi_N$, is [24]: $E = \pm\Delta\sqrt{1 - D \cdot \sin^2(\phi/2)}$, where D is the average transmission probability. There is a general relation between the current through the Andreev state and the phase dispersion of the energy of the Andreev state, $I_s = (2e/\hbar)dE/d\phi$. This equation can be derived directly from the Bogoliubov-deGennes equation or deduced from the thermodynamical equation by using a microscopic expression for the junction free energy [9, 23, 25]. The total supercurrent is given by a summation over the contributions of the current-carrying states which all depend on the phase difference between the two superconductors. These notions are used to calculate the junction properties in the different layouts at the nanoscale.

Something special happens with Andreev reflection for graphene/superconductor (G/S) interfaces, because of the unusual electronic properties of the charge carriers in graphene (no Fermi surface at zero doping and conical band structure) [25]. Differently from the usual case, where the electron and hole both lie in the conduction band, at a G/S interface specular AR occurs if an electron in the conduction band is converted into a hole in the valence band. In undoped graphene, when $E_{\mathrm{F}} = 0$, Andreev reflection is interband at all excitation energies. This has obvious consequences for the Josephson coupling [25].

Junctions with graphene barriers fall within the emerging category of hybrid devices, also in the sense that the barrier is not a thin film but an exfoliated flake. Hybrid in this context may also be interpreted as prebuilt components of the junctions, produced via different techniques and mechanically assembled in the last stage of fabrication. S-NW-S junctions have for instance been proposed as host and sensor of phenomena associated with the presence of Majorana fermions [26–29]. Majorana fermions enable the tunneling of single electrons (with a larger probability $D^{1/2}$). The switch

from 2e to e as the unit of transferred charge between the superconductors amounts to a doubling of the fundamental periodicity of the Josephson energy, from E $\propto \cos \phi$ to E $\propto \cos(\phi/2)$ [28, 29]. In contrast to ordinary Josephson currents, this contribution reflects tunneling of half of a Cooper pair across the junction. Such a fractional Josephson effect was later established in other systems supporting Majorana modes and in direct junctions between p-wave superconductors.

10.2.2 I-V characteristics and phase dynamics, the Resistively Shunted Junction Model

I-V curves are the first imprinting of the nature of the junction. We briefly summarize some standard arguments based on the Resistively and Capacitively Shunted Junction (RCSJ) model, first introduced by McCumber and Stewart [30, 31] to classify some of the I-V curves more commonly observed in experiments. For greater detail we refer the reader to traditional textbooks and reviews [2, 3]. Representing the displacement current by a capacitor (C) and the sum of the quasiparticle and insulator leakage current by a resistance R, we can devise an equivalent circuit for the junction (see Figure 10.4a):

$$I + I_N = I_c \sin(\phi) + V/R + CdV/dt \tag{10.5}$$

The noise source I_N is associated with its shunt resistance. A wide variety of I-V characteristics can be described through an opportune choice of the parameters. We can therefore pass from a regime where capacitance plays a marginal role and no hysteretic behavior is present (see Figure 10.3a) to a tunnel-like behavior with high values of the capacitance, characterized by a hysteretic behavior and by the presence of switching currents (see Figure 10.3b).

This behavior is characteristic of tunnel junctions, and hysteresis is directly associated with the dielectric nature of the barrier and its capacitance (underdamped regime). The switch from the superconducting (S) to the normal state resistive (N) branch follows a distinctive distribution, a direct consequence of fundamental fluctuation processes influenced by dissipation (see Subsection 10.2.2.1). Hysteresis can be incomplete with finite retrapping currents depending on dissipation (see for example Figure 10.3c), with qualitatively different leakage currents, and the possible presence of subgap step structures. Indications on the damping of the junctions are obtained from the resistance, which may depend on the voltage (Figure 10.3c) and on the frequency [32, 33]. The reference value R_n is the normal state value at voltages much higher than the gap value. Let us indicate with Δ_{sw} the voltage value appearing in the junction after the switch from the S branch to the N state. Δ_{sw} does not necessarily correspond to the sum of the gap values of the electrodes as in the ideal tunnel case, because of a less ideal barrier generating additional competing transport mechanisms. A series of other anomalies can appear in the I-V curves such as for instance the pres-

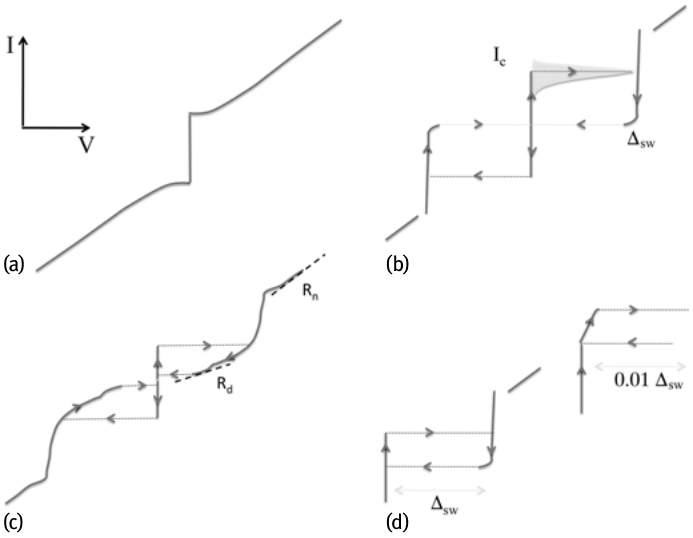

Fig. 10.3: I-V curves of overdamped (a) and underdamped (b) junctions. The (b) behavior is characteristic of tunnel junctions, and hysteresis is directly associated with the dielectric nature of the barrier and its capacitance. The switch from the S to the N branch follows a peculiar distribution indicated in (b) (see the text and Subsection 10.2.2.1). (c) Hysteresis can be incomplete with finite retrapping currents depending on dissipation and accompanied by voltage-dependent leakage currents. (d) For moderately damped junctions (phase diffusion regime) a low-voltage state appears before the switch to the normal state (inset of d, note the voltage scale). The current dependence of the voltage in the diffusion state prior to switching is directly related to the shape of the dissipation barrier (see the text).

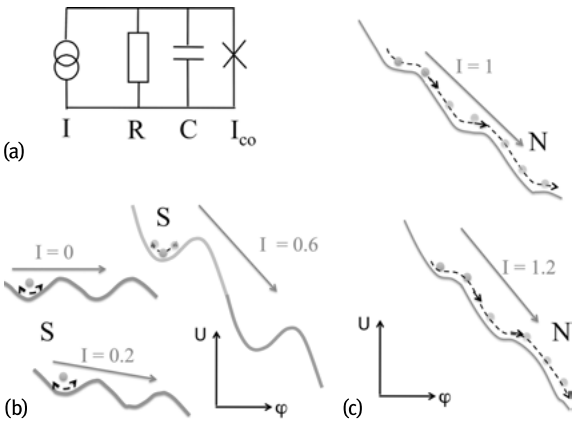

Fig. 10.4: (a) Equivalent circuit of a real Josephson junction with a current bias; (b) and (c) washboard potential for different values of the bias current.

ence of the excess current I_{ex}. I_{ex} is defined as the current axis intercept obtained by extrapolating the linear part of the I-V characteristics for large voltages [3, 34].

Neglecting the noise term and setting $V = \hbar/2e \cdot (\partial\phi/\partial t)$ in Equation (10.5), we obtain:

$$I = \frac{\Phi_0}{2\pi} C \frac{\partial^2 \phi}{\partial t^2} + \frac{\Phi_0}{2\pi} \frac{1}{R} \frac{\partial \phi}{\partial t} + I_c \sin(\phi) \tag{10.6}$$

which can be expressed as:

$$\left(\frac{\Phi_0}{2\pi}\right)^2 C \frac{\partial^2 \phi}{\partial t^2} + \left(\frac{\Phi_0}{2\pi}\right)^2 \frac{1}{R} \frac{\partial \phi}{\partial t} + \frac{\partial}{\partial \phi} U = 0 \tag{10.7}$$

where

$$U = -\Phi_0/(2\pi)(I_c \cos(\phi) + I\phi) \, . \tag{10.8}$$

Considerable insights into the nonlinear dynamics of the junction can be gained by realizing that this equation describes the motion of a ball moving on the tilted washboard potential U [30, 31]. The term involving C represents the mass of the particle, the $1/R$ term represents the damping of the motion, and the average tilt of the washboard is proportional to I. Damping is however strongly influenced by the environment, i.e., the circuitry connected to the junction and some aspects will be discussed in the next section.

For values of $I < I_c$, the particle is confined to one of the potential wells, where it oscillates back and forth at the plasma frequency $\omega_p = (2\pi I_c/\Phi_0 C)^{1/2}(1 - (I/I_c)^2)^{1/4}$ (see Figure 10.4b), which can also be seen as the electrical resonance of the junction capacitance, C, with the mechanical Josephson inductance of the junction, $L_J = \Phi_0/(2\pi I_c)$. In this case the average voltage across the junction is zero. When the current I exceeds I_c, the particle rolls down the washboard (see Figure 10.4c); in this case a voltage appears across the junction.

The McCumber–Stewart damping parameter $\beta_c = 2\pi I_c R^2 C/\Phi_0$ determines the amount of damping [2, 3]. The strength of the friction is also commonly expressed through the junction quality factor $Q = \omega_p RC = (\beta_c)^{1/2}$. While ω_p does not depend on the size of the junctions, Q decreases with the area of the junction, since the effective resistance R is mostly dominated by the high-frequency impedance of the circuit the junction is embedded into (see Subsection 10.2.2.1). Junctions are underdamped, with hysteretic I-V curves, and hence latching for $\beta_c > 1$. For $\beta_c < 1$ they are overdamped, with nonhysteretic I-V, and nonlatching. For hysteretic junctions the nature of the switch from the superconducting to the resistive branch requires more refined analysis, as demonstrated by measurements of the switching current distributions, commonly used for the demonstration of macroscopic quantum phenomena (see Subsection 10.2.2.1).

10.2.2.1 Phase dynamics from thermal activation to macroscopic quantum tunneling

A closer inspection of the washboard potential allows one to understand basic macroscopic quantum phenomena [35], which are relevant to establishing how the junction is coupled to the environment. These studies are relevant for the development of qubits. All fundamental concepts from the notion of tunneling processes in the washboard potential to the real measurement of the switching current distribution (SCD), and the study of the behavior of its first and second momenta (the mean $\overline{I}$ and the width σ) are illustrated in the "flowchart" of the SCD measurements in Figure 10.5. Two distinct typical examples of SCDs are given in Figure 10.5b and e as a function of the temperature T. The widths σ are finally reported as a function of T (Figure 10.5c and f). These two cases summarize different phase dynamics processes, which are the main target of this chapter and are represented in Figure 10.5d and g, respectively.

When ramping the bias current I, the tilt of the energy potential increases and the height $\Delta U(I) = 4\sqrt{2}/3 \cdot E_J(1 - I/I_c)^{3/2}$ of the energy barrier between consecutive wells decreases (see Figure 10.5d). Because of effects of thermal fluctuations and quantum tunneling the junction may switch to the finite voltage state for values of $I < I_c$. The relative weight of these two escape processes depends on the temperature of the system. For $k_B T \gg \hbar\omega_p$, the escape process is dominated by Thermal Activation (TA) (black dashed line in Figure 10.5d) with a rate [36]:

$$\Gamma_T(I) = a_T \frac{\omega_p(I)}{2\pi} \exp\left(-\frac{\Delta U(I)}{k_B T}\right), \tag{10.9}$$

where $a_T \simeq 4\left[(1 + Qk_B T/1.8\Delta U)^{1/2} + 1\right]^{-2}$ is a prefactor of the order of one. At low enough temperatures the escape is dominated by Macroscopic Quantum Tunneling (MQT) (blue dashed curve in Figure 10.5d) with a rate [37]:

$$\Gamma_q(I) = a_q \frac{\omega_p(I)}{2\pi} \exp\left[-7.2 \frac{\Delta U(I)}{\hbar\omega_p}\left(1 + \frac{0.87}{Q}\right)\right] \tag{10.10}$$

with $a_q = 864\pi\Delta U/\hbar\omega_p$. Once the phase particle overcomes the barrier by fluctuations, it keeps running, provided that the damping is below some critical value. The escape from this metastable state corresponds to the appearance of a finite voltage across the junction and the particle runs down the washboard potential with a damping Q^{-1}. The transition to the running state (see Figure 10.5d) only occurs if the kinetic energy gained by the phase particle running down the tilted washboard potential is not all dissipated, but enough energy remains to carry the phase over the next barrier. This occurs if the junction is in the underdamped regime ($Q \gg 1$) [32, 38].

In the moderately damped regime ($1 < Q < 5$), which commonly occurs in junctions of reduced dimensions with small values of I_c, following an escape event the particle may travel down the potential for a few wells and then be retrapped in one of the following minima of the potential (Figure 10.5g) [33]. The analytical expression for

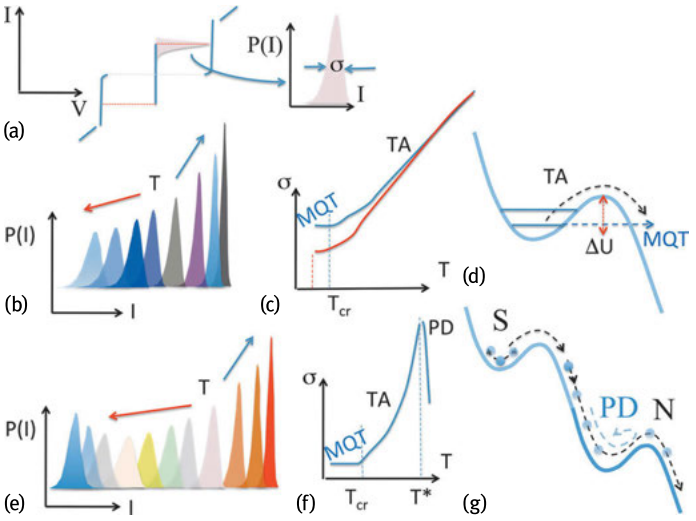

Fig. 10.5: The SCDs are reported as a function of temperature in (b) and (e). They are extracted from hysteretic I-V curves as shown in (a). The different temperature evolutions of the SCDs translate in characteristic dependence of the widths σ of the distributions, as reported in (c) and (f), respectively. (d) The particle/phase overcomes the barrier by Thermal Activation (TA) or by Macroscopic Quantum Tunneling (MQT), then it rolls in the running state. T_{cr} signals the crossover between the TA and the MQT regimes and is tuned by the magnetic field (see text for details). (g) Retrapping processes may occur for intermediate levels of dissipation determining a phase diffusion (PD) regime. T^* separates TA from PD.

the retrapping rate is given by:

$$\Gamma_r(I) = \omega_p \frac{I - I_r}{I_c} \left(\frac{E_J}{2\pi k_B T} \right)^{1/2} \exp\left[-\frac{E_J Q^2}{2k_B T} \left(\frac{I - I_r}{I_c} \right)^2 \right] \tag{10.11}$$

where $I_r = 4I_c/\pi Q$ is the retrapping current in absence of thermal fluctuations [30]. At low bias the process of escape and retrapping may occur multiple times generating diffusion of the phase (Figure 10.5g) until an increase of the tilt of the potential, due to a change in the bias current, raises the velocity of the particle and the transition to the running state occurs. This is known as the Phase Diffusion (PD) regime [33]. The measured distribution of the switching probability $P(I)$ is used to compute the escape rate out of the zero-voltage state as a function of the bias current [39]:

$$\Gamma(I) = \frac{1}{\Delta I} \frac{dI}{dt} ln \left(\frac{\sum_{i \geq I} P(I)}{\sum_{i \geq I + \Delta I} P(I)} \right) \tag{10.12}$$

where dI/dt is the current ramp rate and ΔI is the channel width of the analog-to-digital converter. In an underdamped junction ($Q > 10$) [38], below a crossover temperature T_{cr} the escape process is due to MQT, marked by a temperature-independent σ, while above T_{cr} the process of escape is due to TA above the potential barrier, with a distinctive increase of σ with temperature as $T^{2/3}$, see Figure 10.5c. The

crossover temperature T_{cr} between the thermal and quantum regimes is given by: $T_{cr} = (\hbar\omega_p/2\pi k_B)\left\{(1 + 1/4Q^2)^{1/2} - 1/2Q\right\}$. A tuning of T_{cr} is a powerful in situ knob to prove MQT. This is commonly realized by applying a magnetic field H which modifies I_c and as a consequence the plasma frequency ω_p, thus tuning T_{cr}. In Figure 10.5c the red curve with a reduced T_{cr} shows variations induced by H on σ.

A detailed experimental protocol has been established to prove the quantum behavior of the phase φ across a JJ and its crossover to the thermal regime [32, 38], used in most later experiments. The relevant parameters of the junction and the dissipation level have been determined in situ in the thermal regime from measurements of resonant activation in the presence of microwaves. Such method still represents the most powerful way to characterize the dissipation level in the underdamped regime. Complex impedance seen by the junction at microwave frequencies because of the bias circuitry, ultimately determines the overall dissipation measured in the experiments.

In moderately damped junctions [33] a transition from the TA to PD regime occurs at a crossover temperature $T^* > T_{cr}$. T^* corresponds to a distinctive change in the sign of the temperature derivative of σ, with $d\sigma/dT > 0$ for $T < T^*$ and $d\sigma/dT < 0$ for $T > T^*$, see Figure 10.5f.

The extension of the basic RCSJ equation (10.7) to include current fluctuations, through a white noise driving force $\xi(t)$ (Langevin equation):

$$\ddot{\varphi} + \dot{\varphi}/Q + dU/d\varphi = \xi(t) \tag{10.13}$$

allows a quantitative treatment also of the PD regime. In this equation the time is normalized to $1/\omega_p$, the plasma frequency at zero bias current. The white noise driving force $\xi(t)$ is such that: $\langle\xi(t)\rangle = 0$; $\langle\xi(t), \xi(t')\rangle = \sqrt{k_B T/QE_J}\,\delta(t - t')$. In a more general approach, the damping parameter Q has a frequency dependence better responding to the need of including external shunting impedance [32]. A phase diagram can be built on the basis of E_J and Q through Monte Carlo simulations. It explains how the transition from the TA to PD regime is controlled by I_c and by the shunting C of the JJ, and how a direct crossover from PD to MQT can take place for moderately damped JJs [40–42]. The considerations above can be extended to a more complicated tilted washboard potential U, where effects related to the presence of a second harmonic in the $I_s(\phi)$ are taken into account. For large values of the second harmonic component the potential has the shape of a double well profile (for details see [42–44]). This is of more interest for instance for *HTS* [43] and ferromagnetic JJs [21, 44].

In nanoscale junctions cross sections and hence capacitance are small. As a consequence phase fluctuations are basically no longer regulated by the junction itself, but by the circuit in which it is embedded. Thus, Josephson phenomena in such junctions strongly depend on the environment. The effective capacitance can for instance incorporate some stray capacitive effect of the leads close to the junction. In other words, in a small unshunted current-biased junction connected to a resistive and capacitive (RC) impedance, the process of switching from a phase diffusion branch to a voltage branch is not dominated by thermal activation over the usual washboard

potential barrier (or quantum tunneling through this barrier) occurring in large area junctions. It is rather due to thermal activation above a more complex dissipation barrier for which an expression can be found in the large friction limit [45].

Phase diffusion phenomena may even appear in I-V curves [46–49] (see Figure 10.3d). Low I_c values lead to small E_J values, which turn out to be comparable with E_c. When E_c is comparable to E_J, it is necessary to go beyond the common approximation used up to now, and the Josephson junction is described by the more general Hamiltonian $\mathcal{H}$ [48],

$$\mathcal{H} = -4E_c \frac{\partial^2}{\partial \phi^2} - E_J \cos \phi \tag{10.14}$$

The value of the ratio $x = E_c/E_J$ is a measure of how strongly the charging energy acts in delocalizing the phase, and is related to the width $\delta\phi$ of the phase wave function. An important consequence of phase delocalization is the existence at very low temperatures of a regime of phase diffusion in which the representative point moves steadily down the tilted-washboard potential in the above-mentioned diffusive motion, without escaping and jumping up to the gap voltage. Such a motion gives rise to a measurable finite slope in the superconducting branch [33, 46–49]. A frequency-dependent damping explains the coexistence of hysteresis and phase diffusion.

10.3 Why scale junctions to the 'nanoscale'? From fabrication to general properties and main parameters

There are several motivations to scale junctions to the submicron and possibly to the nanoscale. In some cases new functionalities and phenomena can arise, for instance mesoscopic and low-dimensional effects.

In other cases this is motivated by the need of reaching well-defined values of the junction parameters. It might be the only way to avoid too large values of I_c or too small values of R_n to match the circuit environment [50]. Reducing the junction size changes the range of junction parameters. I_c decreases while R_n increases, but scaling ultimately depends on barrier uniformity. The total capacitance of the Josephson junctions depends not only on the junction area and barrier material, but also on the immediate surroundings of the junction, which adds parasitic capacitance. Especially in the case of extremely small junction areas this parasitic capacitance can dominate the total capacitance. Submicron dimensions are also the strategy to increase clock frequency and integration density for superconducting digital electronic circuits. So, e.g., at a current density J_c of 100 kA/cm^2 the junction area has to be in the range of 0.1 μm^2 compared to 10 μm^2 at 1 kA/cm^2. Scaling to submicron or smaller scales is also important for special applications in metrology, qubits or single charge tunneling devices. The first submicron S-I-S-type tunnel junctions were prepared by an aluminum shadow evaporation technique [50, 51]. Several modified processes were

developed in order to fabricate JJs with submicron tunneling areas, including HTS. The chemical-mechanical polishing (CMP) technique [50, 52] was an important contribution to solving the isolation problem and to strongly improving the quality of wiring connections by minimizing the step heights in circuits with a large number of layers. Keeping in mind that $I_c L \approx \Phi_0$ [53] and it is hard to fabricate a loop with a low inductance, I_c should not exceed a few tens to a few hundreds μA (at the same time the Josephson coupling energy, i.e., I_c, should surpass the thermal noise energy). To fulfill this demand, junctions with submicron size are required. Submicron size lines and junctions may be of advantage in HTS components and circuits. To scale junctions to the submicron range for HTS JJs is particularly important to better isolate specific transport channels and mechanisms. The various transport modes are averaged out by impurities of variable size, by faceting and by local inhomogeneities. The scaling of junctions to the deep submicron is a great chance to improve yield, homogeneity and reproducibility of the junctions, and to have access to the intrinsic properties of HTS JJs with a series of potential advantages. A GB is inhomogeneous in several length scales and some disturbing defects may be avoided by using small dimensions.

In other cases junctions exist only at the nanoscale, when for instance the barrier is a nanowire or a flake of graphene or topological insulator.

10.3.1 Fabrication

Electron beam lithography is the key towards the realization of submicron and nanoscale junctions. It will drive choices for all technologies which cooperate to fabricate the devices, from lift-off to the materials used for the masks, and so on. Fabrication procedures for the realization of nano-SQUIDs, of single-electron transistors (SETs) and even of the more challenging Cooper pair box used for the realization of qubits [54–56] are well consolidated on some materials and for some processing. It is obvious that every nanoscale device is the magic result of a series of nanotechnological processes which will respond differently to the various materials and depend on the layout of the device, thus generating a proliferation of specific recipes.

Another type of tool is the Focussed Ion Beam (FIB). This is used to remove part of the material and takes advantage of the small size of the beam and of the possibility to orient the beam to pattern a large variety of bridges and junctions. It is used for instance for HTS intrinsic Josephson junctions (see Figure 10.1g and Chapter 12).

10.3.2 Hybrid coplanar structures: from 2d-gas to graphene and topological insulator barriers

When we use the term superconducting hybrid device, we traditionally mean a coplanar structure upon which a barrier with special functions, such as for instance

a semiconductor (Sm), was deposited and treated prior to the patterning of the superconducting banks. This junction configuration avoids the extremely challenging critical step of Sm deposition on the superconducting film, and better exploits the capability of growing multilayered Sm heterostructures with high control of the doping level of each single layer. Among the semiconductors, $In_xGa_{1-x}As$ and especially InAs are the most used because they favor more transparent rather than Schottky barriers [57]. In S-Sm-S systems, interface effects and boundary conditions will eventually tune the superconducting proximity effect and the capability of transferring coherence from the electrodes to the barrier [2]. The induced coherence length in the semiconducting barrier ξ_{sm} depends on the carrier density through the diffusion constant and can be tuned, for instance, through a gate voltage for a high transmittance S-Sm interface [2, 57, 58]. These barriers are commonly schematized as two-dimensional electron gas (2DEG) systems and can be tuned through the gate from the weak localization to the strongly localized regime. The values of I_c and R_n can be adjusted in a wide range which covers about three orders of magnitude by applying 20 V [58]. The gate voltage strongly modifies I-V curves and the amplitude of the hysteresis. One of the ultimate targets for this type of device with an Sm barrier has always been the challenging realization of a superconducting Josephson field-effect transistor (Jo-FET) [59].

Of recent conception are all layouts employing flakes of graphene and topological insulators (TI) [60–66] (see Figure 10.1d), and nanotubes [67, 68] and nanowires (InAs, Ge, ...) [70–73] (see Figure 10.1e) as barriers. The ability to handle flakes and nanowires combined with the possibility of nanopatterning has paved the way to the realization of these new families of hybrid Josephson junctions. Epitaxial HgTe layers for instance may readily be turned into a topological insulator by inducing strain in the material [64]. In contrast to Bi compounds, such materials exhibit no bulk conductance. These junctions do not have any immediate impact on applications in superconducting electronics, but are of relevance because they allow us to explore new types of interfaces with possibly unique properties and potentials. The use of these junctions as potential 'sources and sensors' of Majorana fermions (MF) and topological states of matter [26–29] is the most fashionable and recent example. If one thinks of the first generation of point contact junctions [2] or of HTS junctions using a single crystal as a counter-electrode [13], one has the idea of how pioneering structures can be very important to promote further developments in specific directions.

In the standard configuration a nanowire (NW) or a flake is placed on a substrate. The sample is then suitably patterned to define through e-beam lithography the regions where superconducting electrodes will be deposited. The surface of the NW or of the flake is gently polished through ion milling or a more drastic chemical etching, a key step for an acceptable barrier transparency. Superconducting contacts according to current technical limits are typically not closer than 60–100 nm for nanowires and for flakes depending on the specific material, its actual microstructure and granularity, and technological handling. Different layouts and materials have been used and some of them are collected in Table 10.1. The table is instructive because it gives a

survey on the employed materials, and of the typical values of I_c and I_cR_n. The range of parameters of the junctions are quite enlarged in hybrid junctions because of Sm. Carrier density can change by orders of magnitude, mesoscopic effects become ubiquitous, Thouless energy and new relevant disorder scales for quantum transport become active terms of comparison (see the references of Table 10.1). I_c values for NW-based junctions never exceed a few μA, and typically range from tens to hundreds of nA. The radius of the NWs "typically ranges" from 50 to 100 nm, while a typical length is about 1 μm. It is not straightforward to estimate J_c because of possible nonuniform distribution of the current at the cross section. This can be even more significant in two-dimensional barriers, which are typically a few microns wide. Here edge current effects and preferential current paths may play a quite relevant role, because of the intrinsic nature of the material in a confined geometry.

In NW-based JJs modulation of I_c is not commonly observed as a function of the magnetic field H, because the small cross section of the NW would require too high values of H to enclose a flux quantum, thus destroying superconductivity in the LTS electrodes (typically Al). Theoretical I_c(H) have been calculated as a function of the size of the barrier as shown for instance in Figure 10.2 [12]. Fraunhofer patterns have been measured in graphene- and TI-flake barriers (see for instance [61, 63, 65]). Here deviations may be due to anomalous current distribution along the barrier, screening currents in the banks confining flux, and possible generation of vortex entities [69]. Shapiro steps have been observed with expected power dependence [70]. The transport parameters of the NW- and flake-barriers combined with the magnitude of I_c and with the dependence of I_c on the electrode distance (barrier length L), suggest for most cases diffusive transport.

Electrodynamics of these junctions is poorly understood because of difficulties in modeling effective capacitance and dissipation of the junctions. Here heating effects may have more dramatic effects because of the lower dimensionality of the system. Hysteresis in I-V curves is controlled by heating nonequilibrium modes rather than a consequence of the capacitance associated with the dielectric nature of the barrier [74, 75]. This can be reasonably inferred from the lack of general consistency of the set of electrodynamical parameters describing the junction [75]. I_c can be relatively low, but J_c can be high.

An alternative design to those described above, has been proposed and realized for HTS [76] and also tested on Al [73, 77]. It can in principle be extended to all materials whose deposition conditions of multilayer structures are delicate. The InAs NW is suspended over the superconducting banks, over a trench, typically a few micron wide and about 100–200 nm long, and is finally electrically connected to the electrodes. The proposed layout circumvents the compatibility problems stemming from the peculiar growth condition requirements of HTS and its coupling with device-quality semiconductors. In fact, the integration of Sm and HTS components takes place at room temperature after suitable surface treatments assembling prebuilt blocks. The ability to connect HTS banks with InAs NWs implies that several technological issues have

Table 10.1: Properties of different types of nanoscale hybrid Josephson junctions. Some more complete sets of data on junctions with barriers of NWs (TI) can be found in [77, Table 1] ([65]), respectively. In most cases Al stands for a bilayer Ti/Al where Ti guarantees a better electrical contact. Data from [78] are taken at $V_{gate} = 35$ V

Type of junction	L (nm)	I_c (nA)(at T, mK)	I_cR_n (μV)	References
Nb/InAs(NW)/Nb	≈ 140	110 (400)	50	[79]
Nb/InN(NW)/Nb	≈ 100	5000(800)	450	[72]
Al/InAs(NW)/Al	from 100 to 450	135 (40)	2–60	[70]
Al/InAs(NW)/Al	140	60 (300)	11	[77]
Al/GeSi/Al	≈ 100	120(60)	200	[71]
Al/Graphene/Al	≈ 400	35 (30)	120	[60]
Al/Graphene/Al	≈ 400	500 (60)	50	[61]
MoRe/Graphene/MoRe	≈ 1500	120 (50)	50	[78]
Al/Carbon NT/Al	≈ 470	3 (30)	20	[67]
Al/Carbon NT/Al	≈ 200	0.06 (35)		[68]
Nb/Bi_2Te_3/Nb	≈ 50 (W = 500 nm)	25 000 (260)	50 (shunted)	[63]
Al/Bi_2Se_3/Al	≈ 300–400	228–1670 (300)	10 (shunted)	[65]
Nb/HgTe/Nb	≈ 200	3800 (25)	200	[80]

been solved and is the basis for further advances [77]. In particular a) trenches of minimum size of the order of 100–150 nm can be successfully created in a very reproducible way without a severe degradation of the properties of YBCO, which is always protected by a thin Au layer in all fabrication steps (the contact between HTS and InAs always needs a thin 'inert' layer of Au of thickness of the order of 10–20 nm to reduce interface contamination); b) an InAs NW can be in situ polished through passivation etching without severe damage to the superconducting YBCO thin film, c) submicrometer rectangular areas can be patterned on InAs NWs suspended on YBCO banks, thus defining the areas for contacts [77]. Further progress on NW positioning is expected in the coming years.

10.3.3 Submicron HTS Josephson junctions, energy scales and mesoscopic effects

Looking at the large amount of data available in the literature, the apparent contrast of several results, or the fact that some predicted phenomena derived from well-established effects have not yet been clearly detected or only intermittently (such as the second harmonic component, time-reversal symmetry breaking, all derived from d-wave order parameter symmetry [6]), the only reasonable explanation is to assume that several different tunneling and diffusive processes are active in the transport, but only the morphology of the barrier and of the GB will discriminate the role of each transport mechanism. The microstructure acts as a filter determining additional

constraints on the various transport modes, and nanostructures may help to isolate the various contributions.

The first studies on bicrystal submicron JJs gave encouraging results such as the reduction of decoherence, the presence of the second harmonic component or of Andreev-bound states [6]. As already mentioned above recently submicron biepitaxial junctions have been realized down to about a few hundreds nm by using both e-beam lithography and C and Ti masking [81]. Yield and reproducibility have been improved at this width scale, junctions exhibit a more uniform barrier and d-wave-induced effects are even more controlled [81]. The low dissipation of the junctions and a much reduced number of facets have also emerged as characteristic features. These achievements pave the way to the ultimate target, i.e., a reproducible, single-facet junction a few hundreds nanometers wide. This classical controllable top-down approach is accompanied by some types of bottom-up technique [82]. The complex growth process may determine self-assembled nanochannels of variable dimensions, ranging typically from 20 to 200 nm. These nanocontacts can be considered self-protected as far as they are enclosed in macroscopic impurities. Even if this very last technique is not ideal on the long range for applications, since it needs an additional critical step to locate the nanobridges and etch the HTS thin film, it can be really helpful to understand the ultimate limit of junction performances and to understand the transport mechanisms. These channels may be the origin of mesoscopic effects with a characteristic Thouless energy of the order of 1 meV [83]. The idea to use the self-protected GB growing in between impurities has been pursued in [82] by using standard e-beam techniques combined with FIB. By using the competition between the superconducting YBCO and the insulating Y_2BaCuO_5 phases during film growth, nanometer-sized GB junctions of the order of 100 nm were formed in the insulating Y_2BaCuO_5 matrix. FIB has also been used to produce nano-SQUIDs employing bicrystal junctions of widths down to 80 nm [84]. One of the next steps to be understood is whether the scale of 100 nm (coming out from the different experiments discussed above) is representative of the intrinsic nature of HTS or not. A matrix of filaments of smaller size, related to the nature of HTS rather than to the macroscopic artifacts formed during the build-up of the GB, could result for instance from intrinsic stripes or from regions where strong correlations are not uniformly distributed along the GB.

Biepitaxial submicron junctions have shown improved uniformity [49, 81]. Most submicron junctions apparently fall in the moderately damped regime without any excess current. It has been found $\Delta_{sw} \approx I_c R_n$ up to about 4 mV [81], with I_c less than a few μA. I_c can be reproducibly controlled down to a few nA with a minimum E_J comparable with the estimated E_c [49]. Evidence for frequency-dependent damping of these devices has been given.

This work follows the observation of MQT for biepitaxial junctions with a lobe of the order parameter facing a node, thus in the presence of low-energy quasiparticles [43], and studies of the phase dynamics in the moderately damped regime [41, 75, 85]. MQT, TA and PD, see Subsection 10.2.2.1, along with the transitions from one

to another regime have been investigated as a function of Q and E_J. T_{cr} from TA to MQT has been found within the temperature range from 50 to 110 mK, with ω_P of the order of 10 GHz and a Q factor ranging from 30 in the underdamped regime [43, 86] to about 1 in the moderately damped regime [41, 85]. Capacitance values range from 60 fF (in JJs based on $(La_{0.3}Sr_{0.7})(Al_{0.65}Ta_{0.35})O_3$ (LSAT) substrate) to about 1 pF (in STO-based JJs). In general, values of specific capacitance of off-axis biepitaxial junctions on STO substrates are about 5×10^{-4} Fcm^{-2}, one order of magnitude larger than those found for LSAT-based junctions [81], thus demonstrating some control on shunt parasitic capacitance.

Single-electron transistors with tunneling resistances in the range from 200 kΩ to 25 MΩ and charging energies E_c in the range 20–200 μeV have been fabricated using biepitaxial junctions [87]. The YBCO island area is defined by the width of the STO wire and the GB nanojunctions, with the electrodes patterned perpendicular to the seed layer. The energy required to add an extra electron depends on the parity (odd/even) of the excess electrons on the island and increases with magnetic field [87] (see Section 10.4).

Novel insights into nonequilibrium effects in high-J_c JJs have been made possible by a comparative study [75, 85]. The lack of self-consistency of the set of junction parameters used to fit experimental data in Nb [88] and Al [74] LTS JJs with high J_c ($J_c > 10^4 - 10^5$A/cm^2) has already raised the question whether conventional tunnel junction circuit models can fully describe high-J_c JJs. The amplitude of the hysteresis in I-V curves is for instance not consistent with the estimated value of the capacitance [75]. The same behavior is frequently observed in HTS JJs. The study of the fluctuations of I_c through SCD has demonstrated that, above some threshold specific of the type of junction, standard Josephson coherence cannot be sustained because too much current is flowing through the specific cross section. Hysteresis is substantially governed by heating nonequilibrium modes which strongly influence I-V curves and drive fluctuation mechanisms [75]. This has a profound influence on the evaluation of dissipation, of Q and of ω_p. A self-consistent set of parameters is able to account to a large extent for the phase dynamics of a HTS JJ, the shape of I-V curves and all their basic features, in complete analogy to what was firmly established in LTS JJs [75].

10.4 Charging effects in ultrasmall junctions

10.4.1 Introduction to single-electron tunneling and parity effect

The Single-Electron Transistor (SET) consists of a normal conducting or superconducting island connected to two electrodes (source and drain) through two tunnel junctions (see Figure 10.6). A gate electrode is capacitively coupled to the island. If the island and the electrodes are made of a normal metal the total charge is well quantized when the resistances R_{j1}, R_{j2} of the tunnel junctions are much larger than the quan-

tum resistance, $R_Q = h/4e^2 \simeq 6.5\,\mathrm{k\Omega}$, and the charging energy, $E_c = e^2/2C_\Sigma \gg k_B T$, with $k_B T$ defining the thermal energy. Here e is the electron charge and C_Σ is the total capacitance of the island defined as the sum of the junction capacitances (C_{j1} and C_{j2}) and gate capacitance (C_g) (see Figure 10.6). If these conditions are realized electrons tunnel one by one on the island and a gate voltage can vary the charge on it.

The electrostatic energy stored in the capacitances of the junctions and in the gate capacitance is given by the simple expression $U(n) = E_c(n - n_g)^2$ with $n_g = C_g V_g/e$ the normalized induced charge, and V_g is the applied potential to the gate electrode. At small source-drain voltages ($V_{sd} \ll E_c/e$) a source-drain current flows only when two neighboring parabolas cross at half-integer induced gate charge values (see red dots in Figure 10.7[a]). At all other gate values charge transport is forbidden since the energy needed to tunnel on or off the island is larger than the supplied bias voltage. As a consequence the current through source and drain I_{sd} in a normal island SET is e-periodic as a function of the gate voltage (see Figure 10.7a, b).

In a mesoscopic island made of a conventional superconductor, instead, the free energy required to add one electron to an island with an even number of excess electrons is enhanced with respect to the odd case because of the presence of a condensate of Cooper pairs and of an energy gap in the excitation spectrum. At very low temperatures the even-odd free-energy difference of the island with an isotropic gap Δ can be written as

$$F(T) = \Delta - k_B T \ln\left(N_{\mathrm{eff}}(T)\right), \tag{10.15}$$

where N_{eff} represents the number of quasiparticle states within the thermal energy $k_B T$ above the gap in the island volume. The resulting energy bands for a SET with a superconducting island including also the even-odd free energy difference is shown in Figure 10.7(c). Here all the odd parabolas are shifted by F in energy with respect to the even parabolas. Therefore, a finite F results in a $2e$ periodic modulation (parity effect) of I_{sd} as a function of the gate-induced charge (Figure 10.7d). One can determine F from the measured I_{sd} as a function of the normalized gate charge [87].

For a conventional superconductor, F decreases with increasing temperature of the island [89] or by independently decreasing the energy gap Δ, for example, by applying an external magnetic field [90] (see Equation (10.15)).

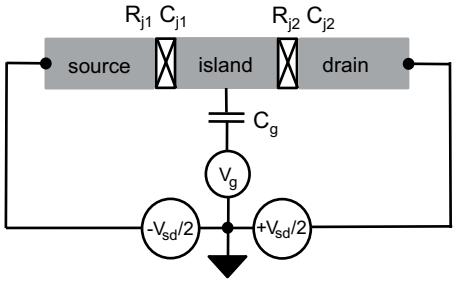

Fig. 10.6: Circuit diagram of a single-electron transistor. The crosses represent the Josephson tunnel junctions characterized by a junction capacitance C_j and resistance R_j. The source-drain current I_{sd} through the single-electron transistor is a function of the source-drain voltage V_{sd} and gate voltage V_g, which is applied through the gate capacitor C_g.

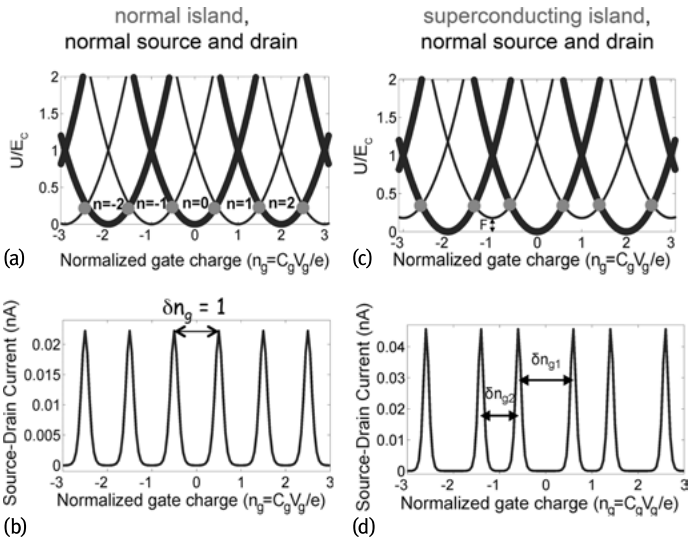

Fig. 10.7: (a) Normalized electrostatic energy as a function of the normalized gate charge n_g for a SET with a normal island. The different parabolas correspond to the number n of added electrons to the island (thin line: odd number n, thick line: even number n). As the gate voltage is changed the energy in the system is minimized by single-electron tunneling events onto and off the island to follow the lowest available parabola. (b) Source-drain current as a function of n_g at a source-drain voltage slightly above zero for a normal metal island. (c) Sum of the normalized electrostatic energy and even-odd energy difference F as a function of n_g for a SET with a superconducting island. Here every odd parabola (thin line) is lifted by the value of F. (d) Source-drain current as a function of n_g at a source-drain bias slightly above 2Δ for a superconducting island. Note that the periodicity of the curve is $2e$ instead of e as for the normal metal island.

A SET is therefore a very powerful tool that allows one to directly measure two characteristic energies in a mesoscopic island: 1) the thermodynamically defined free energy difference F between even and odd number of electrons on the island, by the detection of the parity effect (bulk property of the island), 2) the island superconductive gap, by the current voltage characteristics of the transistor as a function of the gate voltage (surface property of the island). While the detection of a gapped surface density of states is straightforward, i.e., by measuring the current voltage characteristic [87], the observation of a gapped bulk density of states through the measurement of F is an extremely challenging task. This is even the case for low critical temperature superconductors (LTSs).

From extensive studies of the parity effect in LTS SETs the mechanisms preventing the observation of an even-odd free energy difference in a fully gapped superconducting island may be classified as follows:

1. overheating of the SET island;
2. quasiparticle poisoning, i.e., nonequilibrium quasiparticles whose origin is still under debate;

3. very long quasiparticle relaxation times;
4. charge noise (which is limiting the energy resolution of the transistor).

Overall the observation of an island free energy difference F is an extremely difficult task because it involves material-related aspects and specifics of the measurement set up (such as high-frequency filtering of the measurement lines). Moreover, the presence of any quasiparticle state at the Fermi energy of the island would prevent the observation of the parity effect. It is therefore not surprising that it has been previously observed only in Al nanoislands [89] and never, for example, in Nb. Indeed comparative studies of Al and Nb SETs suggested that the elusiveness of parity effects is related to the material properties, in particular the formation of a surface oxide layer under ambient conditions [91, 92]. While Al tends to form a few nanometer-thick insulating oxide layer, niobium is prone to oxidize forming metallic NbOx compounds. This process then leads to localized metallic states in the island, which prevents parity control.

The measurement of an odd-even free energy for unconventional superconductors and/or more complex metal superconductors used for hybrid devices can have groundbreaking implications because of the thermodynamical nature of the single-electron tunneling phenomenon probing the lowest energy state of the island. Very recently the parity effect has been observed in more complex superconductors like an NbTiN island coupled to Al electrodes [93]. The NbTiN compound forms transparent contacts with spin-orbit coupled semiconductor nanowires [27], and has become a preferred superconductor to investigate topological superconductivity and Majorana bound states. The observation of long lifetimes for the parity effect in such a superconductor, exceeding the order of magnitude of the required gate time for the manipulation and braiding of Majorana fermions [94] has strong implications for topological quantum computing.

10.4.2 Unconventional parity effect in $d_{x^2-y^2}$ superconductors

A few years ago the parity effect was also observed in YBCO $d_{x^2-y^2}$ superconductors. This was quite unexpected, since in cuprate superconductors the presence of nodes, together with effects due to disorder and scattering, results in a finite quasiparticle density of states even at zero energy [95]. Therefore there should be no gain in energy by the recombination of unpaired electrons as instead happens for conventional superconductors. Instead it came rather as a surprise the observation of a parity effect in a (103) YBCO island separated by the (001) YBCO oriented electrodes by grain boundary junctions (see Figure 10.8).

The explanation of this experimental result requires a fully gapped superconductivity which can be achieved, in cuprate superconductors, by considering an additional imaginary subdominant order parameter of the type is, or id_{xy}, which allows one to recover a full gap and therefore a parity-dependent free energy. Surprisingly,

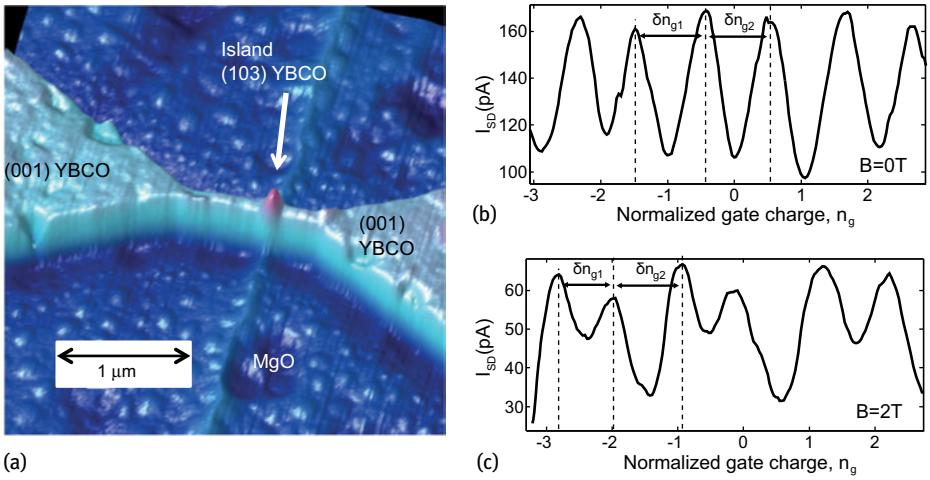

Fig. 10.8: (a) AFM image of a YBCO SET. (b) Source-drain current as a function of the normalized induced charge at zero applied magnetic field. (c) Source-drain current as a function of the normalized induced charge of an externally applied field of 2 T. The 2*e* periodicity clearly demonstrates the occurrence of a fully developed superconducting gap. For comparison see Figure 10.7d.

the parity effect increases with magnetic field rather than being reduced as for conventional superconductors (from Equation (10.15) a reduction of Δ due to a magnetic field would reduce the value of F). This unconventional parity effect is a peculiar feature of a YBCO island and certainly needs more study to be properly understood. It may be possibly related to an imaginary order parameter, which lowers the energy of the ground state of the system, predicted to appear in the presence of a local charge density wave order (CDW) [96]. CDW has been demonstrated in all cuprate families both hole [97] and electron [98] doped. This local order is enhanced in underdoped HTS systems, like the (103) island forming the SET, and in the presence of a magnetic field. It is therefore possible that the associated imaginary superconducting order parameter also increases with an applied magnetic field B giving higher values of F in the field. This experiment gives an account of how a SET transistor can be considered a very powerful spectroscopic tool at the nanoscale allowing us to obtain an energy resolution orders of magnitude better than any other technique [87]. It has been fundamental to detect the appearance of a full superconductive gap in an underdoped YBCO island and may be instrumental in studying evolution in a magnetic field of the superconducting ground state in YBCO nanodots with different dopings and size. These studies could be instrumental to obtaining clear answers about the hierarchy of different competing/cooperating local orders in HTS cuprates, possibly helping us to uncover the microscopic origin of HTS.

10.5 Conclusions

We have revisited some key concepts and some of the most recent advances in the physics of Josephson junctions. Progress in material science and nanotechnology has allowed us to enlarge the 'parameter space' of the Josephson junctions to unprecedented values and control. The continuous progress in well-established LTS JJs consolidates expectations for a series of applications, while unconventional junctions keep opening up novel interesting problems.

Acknowledgment: We gratefully acknowledge valuable contributions by David Gustafsson, Procolo Lucignano, Daniela Stornaiuolo and Arturo Tagliacozzo. This work was partially funded by the Swedish Research Council (VR) and the Knut and Alice Wallenberg Foundation (KAW).

Bibliography

[1] Josephson BD. Possible new effects in superconductive tunnelling. Phys. Lett., 1(7):251–253, 1962.
[2] Barone A, Paternó G. Physics and Appplications of the Josephson Effect. John Wiley & Sons, Inc. New York, NY, USA, 1982.
[3] Likharev KK. Dynamics of Josephson Junctions and Circuits. Gordon and Breach, New York, USA, 1986.
[4] Gurvitch M, Washington MA, Huggins HA. High quality refractory Josephson tunnel junctions utilizing thin aluminum layers. Appl. Phys. Lett., 42(5):472–474, 1983.
[5] Hilgenkamp H, Mannhart J. Grain boundaries in high-T_c superconductors. Rev. Mod. Phys. 74:485–549, 2002.
[6] Tafuri F, Kirtley JR. Weak links in high critical temperature superconductors. Rep. Prog. Phys., 68(11):2573–2663, 2005.
[7] Andreev AF. The thermal conductivity of the intermediate state in superconductors. Zh. Eksp. Teor. Fiz., 46:1823–1828, 1964 [Sov. Phys. JETP 19:1228–1231, 1964].
[8] Likharev KK. Superconducting weak links. Rev. Mod. Phys. 51:101–159, 1979.
[9] Golubov AA, Kupriyanov MYu, Il'ichev E. The current-phase relation in Josephson junctions. Rev. Mod. Phys. 76:411–469, 2004.
[10] Bretheau L, Girit CO, Pothier H, Esteve D, Urbina C. Exciting Andreev pairs in a superconducting atomic contact. Nature, 499(7458):312–315, 2013.
[11] Tsuei CC, Kirtley JR. Pairing symmetry in cuprate superconductors. Rev. Mod. Phys. 72:969–1016, 2000.
[12] Bergeret FS, Cuevas JC. The vortex state and Josephson critical current of diffusive SNS junction. J. Low Temp. Phys., 153(5–6):304–324, 2008.
[13] Van Harlingen DJ. Phase-sensitive tests of the symmetry of the pairing state in the high-temperature superconductors – evidence for $d_{x^2-y^2}$ symmetry. Rev. Mod. Phys. 67:515–535, 1995.
[14] Kirtley JR, Moler KA, Scalapino DJ. Spontaneous flux and magnetic-interference patterns in 0-π Josephson junctions. Phys. Rev. B 56:886–891, 1997.

[15] Smilde HJH, Golubov AA, Ariando, Rijnders G, Dekkers JM, Harkema S, Blank DHA, Rogalla H, Hilgenkamp H. Admixtures to *d*-wave gap symmetry in untwinned $YBa_2Cu_3O_7$ superconducting films measured by angle-resolved electron tunneling. Phys. Rev. Lett. 95:257001, 2005.
[16] Brandt EH, Clem JR. Superconducting thin rings with finite penetration depth. Phys. Rev. B 69:184509, 2004.
[17] Rosenthal PA, Beasley MR, Char K, Colclough MS, Zaharchuk G. Flux focusing effects in planar thin film grain boundary Josephson junctions. Appl. Phys. Lett., 59(26):3482–3484, 1991.
[18] Lindström T, Johansson J, Bauch T, Stepantsov E, Lombardi F, Charlebois SA. Josephson dynamics of bicrystal *d*-wave $YBa_2Cu_3O_{7-\delta}$ dc-squids. Phys. Rev. B 74:014503, 2006.
[19] Lombardi F, Bauch T, Johansson J, Cedergren K, Lindström T, Tafuri F, Stepantsov E. Quantum properties of d-wave $YBa_2Cu_3O_{7-\delta}$ Josephson junction. Physica C: Superconductivity and its Applications 435:8, 2006.
[20] Senapati K, Blamire MG, Barber ZH. Spin-filter Josephson junctions. Nat. Mater., 10(11):849–852, 2011.
[21] Massarotti D, Pal A, Rotoli G, Longobardi L, Blamire MG, Tafuri F. Macroscopic quantum tunnelling in spin filter ferromagnetic Josephson junctions. Nat. Commun. 6:06, 2015.
[22] Blonder GE, Tinkham M, Klapwijk TM. Transition from metallic to tunneling regimes in superconducting microconstrictions: Excess current, charge imbalance, and supercurrent conversion. Phys. Rev. B 25:4515–4532, 1982.
[23] Beenakker CWJ. Random-matrix theory of quantum transport. Rev. Mod. Phys. 69:731–808, 1997.
[24] Kulik IO. Macroscopic quantization and the proximity effect in S-N-S junctions. Zh. Eksp. Teor. Fiz.(Sov. Phys. JETP), 57 (30):1745–1759 (944–950, 1969.
[25] Beenakker CWJ. Colloquium: Andreev reflection and Klein tunneling in graphene. Rev. Mod. Phys. 80:1337–1354, 2008.
[26] Fu L, Kane CL. Superconducting proximity effect and Majorana fermions at the surface of a topological insulator. Phys. Rev. Lett. 100:096407, 2008.
[27] Mourik V, Zuo K, Frolov SM, Plissard SR, Bakkers EPAM, Kouwenhoven LP. Signatures of Majorana fermions in hybrid superconductor-semiconductor nanowire devices. Science, 336(6084):1003–1007, 2012.
[28] Beenakker CWJ. Random-matrix theory of Majorana fermions and topological superconductors. Rev. Mod. Phys. 87:1037–1066, 2015.
[29] Alicea J. New directions in the pursuit of Majorana fermions in solid state systems. Rep. Prog. Phys., 75(7):076501, 2012.
[30] Stewart WC. Current-voltage characteristics of Josephson junctions. Appl. Phys. Lett., 12(8):277–280, 1968.
[31] McCumber DE. Effect of ac impedance on dc voltage-current characteristics of superconductor weak-link junctions. J. Appl. Phys., 39(7):3113–3118, 1968.
[32] Martinis JM, Devoret MH, Clarke J. Experimental tests for the quantum behavior of a macroscopic degree of freedom: The phase difference across a Josephson junction. Phys. Rev. B 35:4682–4698, 1987.
[33] Kautz RL, Martinis JM. Noise-affected I-V curves in small hysteretic Josephson junctions. Phys. Rev. B 42:9903–9937, 1990.
[34] Kleinsasser AW. Excess currents and voltages in superconducting junctions. Appl. Phys. Lett., 62(2):193–195, 1993.
[35] Leggett AJ. Macroscopic quantum systems and the quantum theory of measurement. Prog. Theor. Phys. Supp. 69:80–100, 1980.
[36] Kramers HA. Brownian motion in a field of force and the diffusion model of chemical reactions. Physica, 7(4):284–304, 1940.

[37] Caldeira AO, Leggett AJ. Influence of dissipation on quantum tunneling in macroscopic systems. Phys. Rev. Lett. 46:211–214, 1981.
[38] Devoret MH, Martinis JM, Clarke J. Measurements of macroscopic quantum tunneling out of the zero-voltage state of a current-biased Josephson junction. Phys. Rev. Lett. 55:1908–1911, 1985.
[39] Fulton TA, Dunkleberger LN. Lifetime of the zero-voltage state in Josephson tunnel junctions. Phys. Rev. B 9:4760–4768, 1974.
[40] Kivioja JM, Nieminen TE, Claudon J, Buisson O, Hekking FWJ, Pekola JP. Observation of transition from escape dynamics to underdamped phase diffusion in a Josephson junction. Phys. Rev. Lett. 94:247002, 2005.
[41] Longobardi L, Massarotti D, Stornaiuolo D, Galletti L, Rotoli G, Lombardi F, Tafuri F. Direct transition from quantum escape to a phase diffusion regime in YBaCuO biepitaxial Josephson junctions. Phys. Rev. Lett. 109:050601, 2012.
[42] Massarotti D, Longobardi L, Galletti L, Stornaiuolo D, Rotoli G, Tafuri F. Macroscopic quantum tunneling and retrapping processes in moderately damped YBaCuO Josephson junctions. Low Temp. Phys., 39(3):294–298, 2013.
[43] Bauch T, Lombardi F, Tafuri F, Barone A, Rotoli G, Delsing P, Claeson T. Macroscopic quantum tunneling in d-wave $YBa_2Cu_3O_{7-x}$ Josephson junctions. Phys. Rev. Lett. 94:087003, 2005.
[44] Sickinger H, Lipman A, Weides M, Mints RG, Kohlstedt H, Koelle D, Kleiner R, Goldobin E. Experimental evidence of a φ Josephson junction. Phys. Rev. Lett. 109:107002, 2012.
[45] Vion D, Aassime A, Cottet A, Joyez P, Pothier H, Urbina C, Esteve D, Devoret MH. Manipulating the quantum state of an electrical circuit. Science, 296(5569):886–889, 2002.
[46] Iansiti M, Tinkham M, Johnson AT, Smith WF, Lobb CJ. Charging effects and quantum properties of small superconducting tunnel junctions. Phys. Rev. B 39:6465–6484, 1989.
[47] Iansiti M, Johnson AT, Smith WF, Rogalla H, Lobb CJ, Tinkham M. Charging energy and phase delocalization in single very small Josephson tunnel junctions. Phys. Rev. Lett. 59:489–492, 1987.
[48] Tinkham M. Introduction to Superconductivity: Second Edition. Dover Publications, 2004.
[49] Stornaiuolo D, Rotoli G, Massarotti D, Carillo F, Longobardi L, Beltram F, Tafuri F. Resolving the effects of frequency-dependent damping and quantum phase diffusion in $YBa_2Cu_3O_{7-x}$ Josephson junctions. Phys. Rev. B 87:134517, 2013.
[50] Anders S, Blamire MG, Buchholz F-Im, Crété D-G, Cristiano R, Febvre P, Fritzsch L, Herr A, Il'ichev E, Kohlmann J, Kunert J, Meyer H-G, Niemeyer J, Ortlepp T, Rogalla H, Schurig T, Siegel M, Stolz R, Tarte E, ter Brake HJM, Toepfer H, Villegier J-C, Zagoskin AM, Zorin AB. European roadmap on superconductive electronics – status and perspectives. Physica C, 470(23–24):2079–2126, 2010.
[51] Dolata R, Scherer H, Zorin AB, Niemeyer J. Single electron transistors with $Nb/AlO_x/Nb$ junctions. J. Vac. Sci. Technol. B, 21(2):775–780, 2003.
[52] Anders S, Schmelz M, Fritzsch L, Stolz R, Zakosarenko V, Schönau T, Meyer H-G. Submicrometer-sized, cross-type $Nb/AlO_x/Nb$ tunnel junctions with low parasitic capacitance. Supercond. Sci. Tech., 22(6):064012, 2009.
[53] ter Brake HJM, Buchholz FIm, Burnell G, Claeson T, Crété D, Febvre P, Gerritsma GJ, Hilgenkamp H, Humphreys R, Ivanov Z, Jutzi W, Khabipov MI, Mannhart J, Meyer HG, Niemeyer J, Ravex A, Rogalla H, Russo M, Satchell J, Siegel M, Töpfer H, Uhlmann FH, Villégier JC, Wikborg E, Winkler D, Zorin AB. Scenet roadmap for superconductor digital electronics. Physica C, 439(1):1–41, 2006.
[54] Clarke J, Wilhelm FK. Superconducting quantum bits. Nature, 453(7198):1031–1042, 2008.
[55] Devoret MH, and Martinis JM, Implementing qubits with superconducting integrated circuits. In Everitt HO. editor, Experimental Aspects of Quantum Computing, pages 163–203. Springer US, 2005.

[56] Devoret MH, Schoelkopf RJ. Superconducting circuits for quantum information: An outlook. Science, 339(6124):1169–1174, 2013.
[57] Kleinsasser AW, Jackson TN. Critical currents of superconducting metal-oxide-semiconductor field-effect transistors. Phys. Rev. B 42:8716–8719, 1990.
[58] Takayanagi H, Hansen JB, Nitta J. Mesoscopic fluctuations of the critical current in a superconductor—normal-conductor—superconductor. Phys. Rev. Lett. 74:166–169, 1995.
[59] Mannhart J. High-T_c transistors. Supercond. Sci. Tech., 9(2):49, 1996.
[60] Heersche HB, Jarillo-Herrero P, Oostinga JB, Vandersypen LMK, Morpurgo AF. Bipolar supercurrent in graphene. Nature, 446(7131):56–59, 2007.
[61] Ojeda-Aristizabal C, Ferrier M, Guéron S, Bouchiat H. Tuning the proximity effect in a superconductor-graphene-superconductor junction. Phys. Rev. B 79:165436, 2009.
[62] Monteverde M, Ojeda-Aristizabal C, Komatsu K, Li C, Ferrier M, Guéron S, Bouchiat H. What are the relevant disorder scales for quantum transport in graphene? J. Low Temp. Phys., 167(1–2):1–14, 2012.
[63] Veldhorst M, Snelder M, Hoek M, Gang T, Guduru VK, Wang XL, Zeitler U, van der Wiel WG, Golubov AA, Hilgenkamp H, Brinkman A. Josephson supercurrent through a topological insulator surface state. Nat. Mater., 11(5):417–421, 2012.
[64] Sochnikov I, Maier L, Watson CA, Kirtley JR, Gould C, Tkachov G, Hankiewicz EM, Brüne C, Buhmann H, Molenkamp LW, Moler KA. Nonsinusoidal current-phase relationship in Josephson junctions from the 3d topological insulator HgTe. Phys. Rev. Lett. 114:066801, 2015.
[65] Galletti L, Charpentier S, Iavarone M, Lucignano P, Massarotti D, Arpaia R, Suzuki Y, Kadowaki K, Bauch T, Tagliacozzo A, Tafuri F, Lombardi F. Influence of topological edge states on the properties of Al/Bi_2Se_3/Al hybrid Josephson devices. Phys. Rev. B 89:134512, 2014.
[66] Kurter C, Finck ADK, Ghaemi P, Hor YS, Van Harlingen DJ. Dynamical gate-tunable supercurrents in topological Josephson junctions. Phys. Rev. B 90:014501, 2014.
[67] Jarillo-Herrero P, van Dam JA, Kouwenhoven LP. Quantum supercurrent transistors in carbon nanotubes. Nature, 439(7079):953–956, 2006.
[68] Cleuziou JP, Wernsdorfer W, Bouchiat V, Ondarcuhu T, Monthioux M. Carbon nanotube superconducting quantum interference device. Nat. Nano., 1(1):53–59, 2006.
[69] Massarotti D, Jouault B, Rouco V, Charpentier S, Bauch T, Michon A, De Candia A, Lucignano P, Lombardi F, Tafuri F, Tagliacozzo A. Incipient Berezinskii–Kosterlitz–Thouless transition in two-dimensional coplanar Josephson junctions. Phys. Rev. B, 94:054525, 2016.
[70] Doh Y-J, van Dam JA, Roest AL, Bakkers EPAM, Kouwenhoven LP, De Franceschi S. Tunable supercurrent through semiconductor nanowires. Science, 309(5732):272–275, 2005.
[71] Xiang J, Vidan A, Tinkham M, Westervelt RM, Lieber CM. Ge/Si nanowire mesoscopic Josephson junctions. Nat. Nano., 1(3):208–213, 2006.
[72] Frielinghaus R, Batov IE, Weides M, Kohlstedt H, Calarco R, Schäpers Th. Josephson supercurrent in Nb/InN-nanowire/Nb junctions. Appl. Phys. Lett., 96(13), 2010.
[73] Abay S, Persson D, Nilsson H, Wu F, Xu HQ, Fogelström M, Shumeiko V, Delsing P. Charge transport in InAs nanowire Josephson junctions. Phys. Rev. B 89:214508, 2014.
[74] Courtois H, Meschke M, Peltonen JT, Pekola JP. Origin of hysteresis in a proximity Josephson junction. Phys. Rev. Lett. 101:067002, 2008.
[75] Massarotti D, Stornaiuolo D, Lucignano P, Galletti L, Born D, Rotoli G, Lombardi F, Longobardi L, Tagliacozzo A, Tafuri F. Breakdown of the escape dynamics in Josephson junctions. Phys. Rev. B 92:054501, 2015.
[76] Baghdadi R, Arpaia R, Charpentier S, Golubev D, Bauch T, Lombardi F. Fabricating nanogaps in $YBa_2Cu_3O_{7-\delta}$ for hybrid proximity-based Josephson junctions. Phys. Rev. Applied 4:014022, 2015.

[77] Montemurro D, Massarotti D, Lucignano P, Roddaro S, Stornaiuolo D, Ercolani D, Sorba L, Tagliacozzo A, Beltram F, Tafuri F. Towards a hybrid high critical temperature superconductor junction with a semiconducting InAs nanowire barrier. J. Supercond. Novel Magn., 28(12):3429–3437, 2015.

[78] Calado VE, Goswami S, Nanda G, Diez M, Akhmerov AR, Watanabe K, Taniguchi T, Klapwijk TM, Vandersypen LMK. Ballistic Josephson junctions in edge-contacted graphene. Nat. Nano., 2015.

[79] Günel HY, Borgwardt N, Batov IE, Hardtdegen H, Sladek K, Panaitov G, Grützmacher D, Schäpers Th. Crossover from Josephson effect to single interface Andreev reflection in asymmetric superconductor/nanowire junctions. Nano Letters, 14(9):4977–4981, 2014. PMID: 25118624.

[80] Oostinga JB, Maier L, Schüffelgen P, Knott D, Ames C, Brüne C, Tkachov G, Buhmann H, Molenkamp LW. Josephson supercurrent through the topological surface states of strained bulk HgTe. Phys. Rev. X, 3(2):021007, 2013.

[81] Stornaiuolo D, Rotoli G, Cedergren K, Born D, Bauch T, Lombardi F, Tafuri F. Submicron YBaCuO biepitaxial Josephson junctions: d-wave effects and phase dynamics. J. Appl. Phys., 107(11), 2010.

[82] Gustafsson D, Pettersson H, Iandolo B, Olsson E, Bauch T, Lombardi F. Soft nanostructuring of YBCO Josephson junctions by phase separation. Nano Letters, 10(12):4824–4829, 2010. PMID: 21080664.

[83] Lucignano P, Stornaiuolo D, Tafuri F, Altshuler BL, Tagliacozzo A. Evidence for a minigap in YBCO grain boundary Josephson junctions. Phys. Rev. Lett. 105:147001, 2010.

[84] Nagel J, Konovalenko KB, Kemmler M, Turad M, Werner R, Kleisz E, Menzel S, Klingeler R, Büchner B, Kleiner R, Koelle D. Resistively shunted $YBa_2Cu_3O_7$ grain boundary junctions and low-noise squids patterned by a focused ion beam down to 80 nm linewidth. Supercond. Sci. Tech., 24(1):015015, 2011.

[85] Massarotti D, Longobardi L, Galletti L, Stornaiuolo D, Montemurro D, Pepe G, Rotoli G, Barone A, Tafuri F. Escape dynamics in moderately damped Josephson junctions. Low Temp. Phys., 38(4):263–272, 2012.

[86] Bauch T, Lindstrom T, Tafuri F, Rotoli G, Delsing P, Claeson T, Lombardi F. Quantum dynamics of a d-wave Josephson junction. Science, 311(5757):57–60, 2006.

[87] Gustafsson D, Golubev D, Fogelstrom M, Claeson T, Kubatkin S, Bauch T, Lombardi F. Fully gapped superconductivity in a nanometre-size YBaCuO island enhanced by a magnetic field. Nat. Nano., 8(1):25–30, 2013.

[88] Kleinsasser AW, Buhrman RA. High-quality submicron niobium tunnel junctions with reactive ion-beam oxidation. Appl. Phys. Lett., 37(9):841–843, 1980.

[89] Tuominen MT, Hergenrother JM, Tighe TS, Tinkham M. Experimental evidence for parity-based 2e periodicity in a superconducting single-electron tunneling transistor. Phys. Rev. Lett. 69:1997–2000, 1992.

[90] Tuominen MT, Hergenrother JM, Tighe TS, Tinkham M. Even-odd electron number effects in a small superconducting island: Magnetic-field dependence. Phys. Rev. B 47:11599–11602, 1993.

[91] Dolata R, Scherer H, Zorin AB, Niemeyer J. Single-charge devices with ultrasmall $Nb/AlO_x/Nb$ trilayer Josephson junctions. J. Appl. Phys., 97(5):054501, 2005.

[92] Savin AM, Meschke M, Pekola JP, Pashkin YuA, Li TF, Im H, Tsai JS. Parity effect in Al and Nb single electron transistors in a tunable environment. Appl. Phys. Lett., 91(6):063512, 2007.

[93] van Woerkom DJ, Geresdi A, Kouwenhoven LP. One minute parity lifetime of a NbTiN Cooper-pair transistor. Nat. Phys., 11(7):547–550, 2015.

[94] Hyart T, van Heck B, Fulga IC, Burrello M, Akhmerov AR, Beenakker CWJ. Flux-controlled quantum computation with Majorana fermions. Phys. Rev. B 88:035121, 2013.

[95] Hussey NE. Low-energy quasiparticles in high-Tc cuprates. Adv. Phys., 51(8):1685–1771, 2002.
[96] Wang Y, Agterberg DF, Chubukov A. Coexistence of charge-density-wave and pair-density-wave orders in underdoped cuprates. Phys. Rev. Lett. 114:197001, 2015.
[97] Ghiringhelli G, Le Tacon M, Minola M, Blanco-Canosa S, Mazzoli C, Brookes NB, De Luca GM, Frano A, Hawthorn DG, He F, Loew T, Moretti Sala M, Peets DC, Salluzzo M, Schierle E, Sutarto R, Sawatzky GA, Weschke E, Keimer B, Braicovich L. Long-range incommensurate charge fluctuations in (Y, Nd)$Ba_2Cu_3O_{6+x}$. Science, 337(6096):821–825, 2012.
[98] da Silva Neto EH, Comin R, He F, Sutarto R, Jiang Y, Greene RL, Sawatzky GA, Damascelli A. Charge ordering in the electron-doped superconductor $Nd_{2-x}Ce_xCuO_4$. Science, 347(6219):282–285, 2015.